Wide supercooled liquid region and soft magnetic properties of Fe56Co7Ni7Zr0-10Nb (or Ta)0-10B20 amorphous alloys

doi: 10.1063/1.366923

Wide supercooled liquid region and soft magnetic properties of $Fe_{56}Co_7Ni_7Zr_{0-10}Nb$ (or Ta)$_{0-10}B_{20}$ amorphous alloys

A. Inoue, H. Koshiba,[a] T. Zhang, and A. Makino[a]
Institute for Materials Research, Tohoku University, Sendai 980-77, Japan

(Received 10 June 1997; accepted for publication 31 October 1997)

An amorphous phase with a wide supercooled liquid region before crystallization was formed in $Fe_{56}Co_7Ni_7Zr_{10-x}M_xB_{20}$ (M=Nb or Ta, $x=0-10$ at. %) alloys by melt spinning. The glass transition temperature (T_g) and crystallization temperature (T_x) increase by the dissolution of 2% M and the degree of the increase is larger for T_x, leading to maximum $\Delta T_x(=T_x-T_g)$ of 85 K at 2% Nb and 87 K at 2% Ta which are larger by about 20 K than the largest value for newly developed Fe–(Al, Ga)–(P,C,B,Si) amorphous alloys. The crystallization of the Nb-containing alloys occurs through two stages of amorphous (Am)$\rightarrow$Am′+α-Fe+γ-Fe+$Fe_{76}Nb_6B_{18}$ $\rightarrow\alpha$-Fe+γ-Fe+$Fe_{76}Nb_6B_{18}$+Fe_2Zr in the range less than about 6% Nb and Am$\rightarrow$Am′ +γ-Fe$\rightarrow\gamma$-Fe+$Co_3Nb_2B_5$+Ni_8Nb in the range above 8% Nb. The change in the crystallization process with Nb content seems to reflect the easy precipitation of γ-Fe by the increase in the number of Fe–Nb pairs with weaker bonding nature as compared with the Fe–Zr pairs. The best soft magnetic properties were obtained at 2% Nb or 8% Ta. The saturation magnetization, coercive force, effective permeability at 1 kHz, and saturated magnetostriction in the annealed state for 300 s at 800 K are, respectively, 0.96 T, 2.0 A/m, 19 100, and 10×10^{-6} for the 10% Zr alloy, 0.75 T, 1.1 A/m, 25 000, and 12×10^{-6} for the 2% Nb alloy, and 0.85 T, 1.5 A/m 17 400, and 14×10^{-6} for the 8% Ta alloy. The Curie temperature is 531 K for the 2% Nb alloy and 538 K for the 8% Ta alloy. The success in synthesizing the new amorphous alloys with the wide supercooled liquid region and good soft magnetic properties is promising for future development as soft magnetic bulk amorphous alloys. © *1998 American Institute of Physics.* [S0021-8979(98)03204-6]

I. INTRODUCTION

The search for an amorphous alloy with a wide supercooled liquid region before crystallization is important because the existence of the supercooled liquid region implies the high thermal stability of the supercooled liquid against crystallization. It is generally known that the high thermal stability enables the fabrication of a bulk amorphous alloy by conventional casting processes. All bulk amorphous alloys in Ln–Al–TM,[1,2] Mg–Ln–TM,[3,4] Zr–Al–TM,[5–7] Zr–(Ti,Nb,Pd)–Al–TM,[8] Zr–Ti–TM–Be,[9] Pd–Cu–Ni–P[10] and Fe–(Al,Ga)–(P,C,B,Si)[11,12] (Ln=lanthanide metal, TM =transition metal) systems exhibit a wide supercooled liquid region exceeding 50 K. The temperature interval of the supercooled liquid region defined by the difference between glass transition temperature (T_g) and crystallization temperature (T_x), $\Delta T_x(=T_x-T_g)$ has been reported to reach 98 K for the Ln-based alloy, 61 K for the Mg-based alloys, 127 K[13] for the Zr-based alloys, 98 K for the Pd-based alloys, and 61 K for the Fe-based alloys. There is a clear tendency for glass-forming ability to increase with increasing ΔT_x. The above-described bulk amorphous alloys always satisfy the following three empirical rules[14–19] for achievement of large glass-forming ability i.e., (1) multicomponent alloy systems consisting of more than three elements, (2) significantly different atomic size ratios above about 12% among the main constituent elements, and (3) negative heats of mixing among their elements. Based on the three empirical rules, we have searched for new Fe-based amorphous alloys with a wider supercooled liquid region before crystallization. As a result, we have found that amorphous alloys with large ΔT_x values reaching about 90 K are formed in multicomponent (Fe,Co,Ni)–Zr–B[20] and Fe–(Co,Ni)–(Zr,Nb)–B[21,22] systems. Besides, the new Fe-based amorphous alloys also exhibit good soft magnetic properties combined with low saturated magnetostriction and are expected to develop as a new type of soft magnetic material which is different from conventional Fe–Si–B and Co–Fe–Si–B amorphous alloys.[23,24] This article is intended to present the compositional dependence of T_g, T_x, ΔT_x, crystallization behavior and magnetic properties for $Fe_{56}Co_7Ni_7Zr_{10-x}Nb_xB_{20}$ and $Fe_{56}Co_7Ni_7Zr_{10-x}Ta_xB_{20}$ amorphous alloys and to investigate the reason for the appearance of the wide supercooled liquid region for the new Fe-based amorphous alloys.

II. EXPERIMENTAL PROCEDURE

Multicomponent alloys with composition $Fe_{56}Co_7Ni_7Zr_{10-x}Nb_xB_{20}$ and $Fe_{56}Co_7Ni_7Zr_{10-x}Ta_xB_{20}$ were examined in the present study because the $Fe_{56}Co_7Ni_7Zr_{10}B_{20}$ amorphous alloy had the widest supercooled liquid region before crystallization. Their master ingots were prepared by arc melting the mixture of pure Fe, Co, Ni, Zr, Nb, and Ta metals and pure B crystal in an argon atmosphere. The alloy compositions represent the nominal atomic percentage of the mixture. Rapidly solidified ribbons

[a]Permanent address: Alps Electric Co. Ltd., Nagaoka 940, Japan.

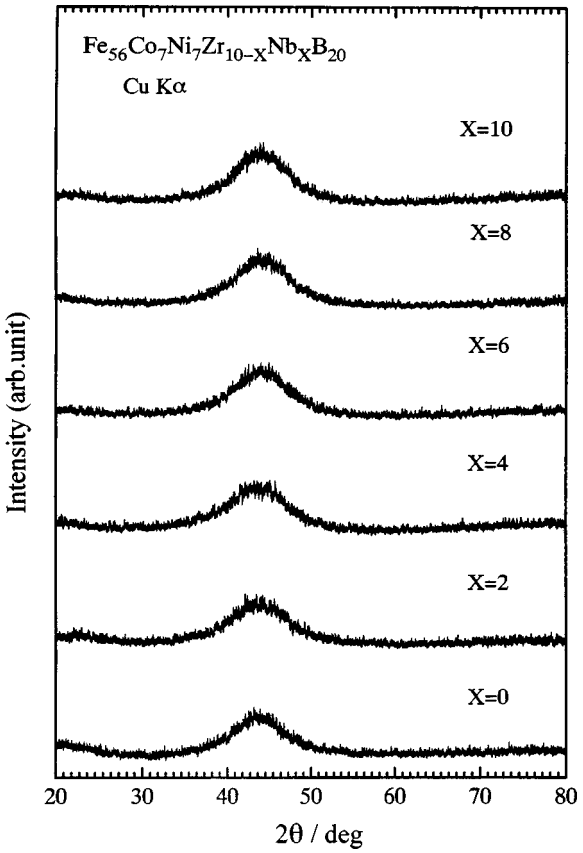

FIG. 1. X-ray diffraction patterns of melt-spun $Fe_{56}Co_7Ni_7Zr_{10-x}Nb_xB_{20}$ ($x=0$, 2, 4, 6, 8, and 10 at. %.) alloys.

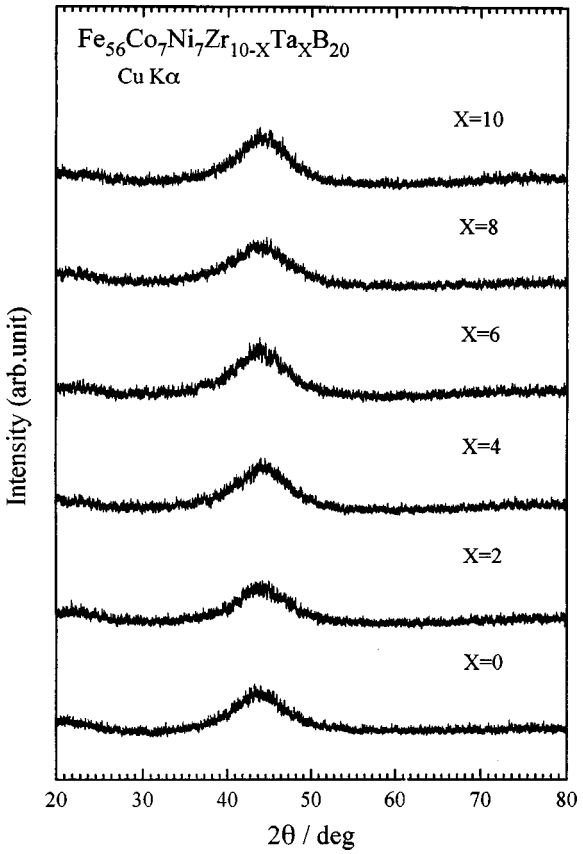

FIG. 2. X-ray diffraction patterns of melt-spun $Fe_{56}Co_7Ni_7Zr_{10-x}Ta_xB_{20}$ ($x=0$, 2, 4, 6, 8, and 10 at. %) alloys.

with a cross section of 0.02×1.0 mm^2 were prepared by melt spinning the master ingots in an argon atmosphere. The amorphous nature was examined by x-ray diffractometry and transmission electron microscopy (TEM). The alloy components of the as-quenched alloys were determined by electron probe microanalysis (EPMA). Thermal stability associated with glass transition, supercooled liquid region, and crystallization was examined at a heating rate of 0.67 K/s by differential scanning calorimetry (DSC). The crystallized structure was examined by high-resolution TEM linked with nanobeam electron diffraction pattern, energy dispersive x-ray spectroscopy (EDXS), and electron energy loss spectroscopy (EELS). Magnetization at room temperature was measured in a maximum applied field of 1260 kA/m with a vibrating sample magnetometer (VSM). Coercive force was measured with a I–H loop tracer. Permeability was evaluated at 1 kHz with an impedance analyzer. Saturated magnetostriction was measured under a field of 240 kA/m by a three-terminal capacitance method. Curie temperature was determined by extrapolating the I-T curve in the constant coupling approximation manner.

III. RESULTS

Figures 1 and 2 show x-ray diffraction patterns of the melt-spun $Fe_{56}Co_7Ni_7Zr_{10-x}Nb_xB_{20}$ and $Fe_{56}Co_7Ni_7Zr_{10-x}Ta_xB_{20}$ ($x=0$, 2, 4, 6, 8, and 10 at .%) alloys, respectively. Only a broad peak is seen at a waver vector ($K_p=4\pi\sin\theta/\lambda$) of about 30.2 nm^{-1} for both alloy systems and no diffraction peak corresponding to a crystalline phase is seen for all the alloys. The x-ray diffraction data indicate clearly that these melt-spun alloys are composed of an amorphous phase without crystallinity. Figure 3 shows DSC curves of the melt-spun $Fe_{56}Co_7Ni_7Zr_{10-x}Nb_xB_{20}$ ($x=0$, 2, 4, 6, 8, and 10 at. %) amorphous alloys. It is to be noticed that a distinct glass transition, followed by a wide supercooled liquid region, is observed in the temperature range before crystallization for all the alloys. Considering that more than two exothermic peaks are seen on the DSC curves, the crystallization appears to take place through multiple stages. The second exothermic peak is more distinct for the 8 and 10 at .% Nb alloys. The similar feature in the glass transition, supercooled liquid, and multiple-stage crystallization is also recognized on the DSC curves of the $Fe_{56}Co_7Ni_7Zr_{10-x}Ta_xB_{20}$ alloys as shown in Fig. 4. Based on these DSC curves, the glass transition temperature (T_g), the onset temperature of the first-stage crystallization peak (T_x), and the temperature interval of supercooled liquid region ($\Delta T_x=T_x-T_g$) for the Fe–Co–Ni–Zr–Nb–B and Fe–Co–Ni–Zr–Ta–B amorphous alloys were plotted as a function of Nb or Ta content in Fig. 5. The T_g and T_x are 814 and 887 K, respectively, for the 0% Nb alloy, increase by the dissolution of Nb or Ta, show maximum values of 828 and 913 K, respectively, for the 2–4% Nb alloys and 827 and 914 K, respectively, for the 2–4% Ta alloys and then decrease significantly with further increasing Nb or Ta content. The degree of the increase is larger for T_x than for T_g, leading to

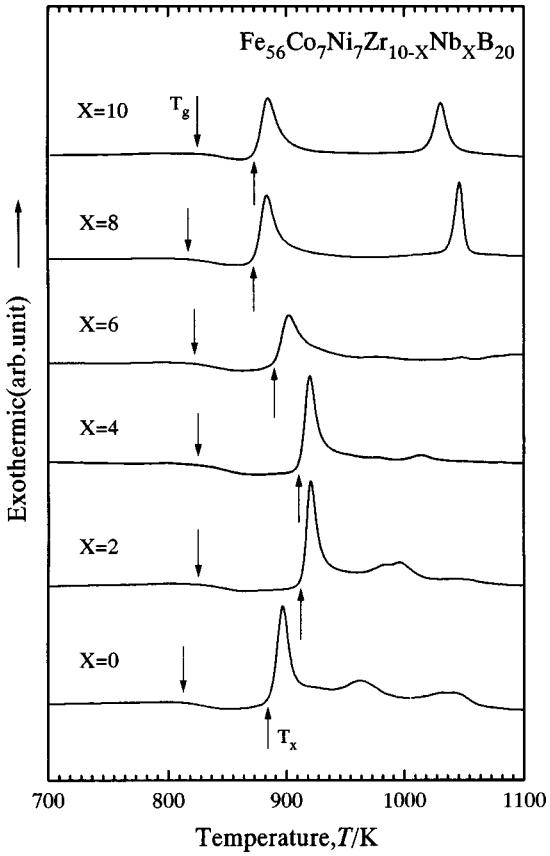

FIG. 3. Differential scanning calorimetric curves of the amorphous $Fe_{56}Co_7Ni_7Zr_{10-x}Nb_xB_{20}$ ($x=0$, 2, 4, 6, 8, and 10 at. %) alloys.

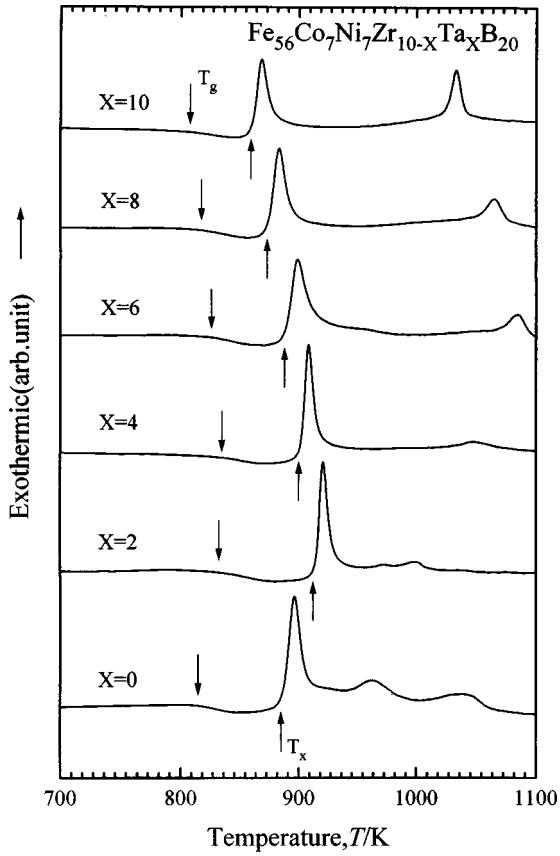

FIG. 4. Differential scanning calorimetric curves of the amorphous $Fe_{56}Co_7Ni_7Zr_{10-x}Ta_xB_{20}$ ($x=0$, 2, 4, 6, 8, and 10 at. %) alloys.

the increase in ΔT_x from 73 K for the 0% Nb alloy to 85 K for the 2% Nb alloy and 87 K for the 2% Ta alloy. Here, it is important to point out that the $Fe_{56}Co_7Ni_7Nb_{10}B_{20}$ and $Fe_{56}Co_7Ni_7Ta_{10}B_{20}$ amorphous alloys also exhibit the glass transition and supercooled liquid region, though the decrease in T_x causes smaller ΔT_x values of 45–57 K.

With the aim of clarifying the reason for the change in the crystallization behavior around 7% Nb or Ta, x-ray diffraction patterns of the $Fe_{56}Co_7Ni_7Zr_{10-x}Nb_xB_{20}$ ($x=2$, 4, 8, and 10 at .%) alloys heated for 600 s at temperatures just above the first and the second exothermic peaks are shown in Fig. 6. The x-ray diffraction patterns were identified to consist of α-Fe, γ-Fe, $Fe_{76}Nb_6B_{18}$, and Fe_2Zr phases for the 2 and 4% Nb alloys heated to 1040 K just above the second exothermic peak, a γ-Fe phase for the 8 and 10% Nb alloys heated to 883 K corresponding to the temperature just above the first exothermic peak, and γ-Fe, $Co_3Nb_2B_5$, and Ni_8Nb phases for the 8 and 10% Nb alloys heated to 1028 to 1047 K just above the second exothermic peak. In order to examine the crystalline phase in the first crystallization stage for the $Fe_{56}Co_7Ni_7Zr_{10-x}Nb_xB_{20}$ alloys containing less than 6 at. % Nb, the x-ray diffraction patterns of the 2% Nb- and 4% Nb-containing alloys annealed for 600 s at 920 K are shown in Fig. 7, together with the data of the alloys annealed at 1040 K. The annealing temperatures of 920 and 1040 K correspond to those just above the first and second exothermic peaks, respectively. The x-ray diffraction peaks of both alloys are identified to be α-Fe, γ-Fe, and $Fe_{76}Nb_6B_{18}$ phases and no appreciable peak of Fe_2Zr is observed. It is therefore said that the crystallization of the Fe–Co–Ni–Zr–Nb–B alloys containing less than 6 at .% Nb also takes place through two stages of amorphous→amorphous $+\alpha$-Fe$+\gamma$-Fe$+Fe_{76}Nb_6B_{18}\rightarrow\alpha$-Fe$+\gamma$-Fe$+Fe_{76}Nb_6B_{18}+Fe_2Zr$. The distinct increase in the second-stage crystallization peak around 6–8 at .% Nb on the DSC curves reflects the change in the second-stage crystalline phase from Fe_2Zr to $Co_3Nb_2B_5+Ni_8Nb$.

Here, it is important to examine the distribution of Co and Ni elements in each constituent phase because the simultaneous addition is effective for the further extension of the supercooled liquid region. Figure 8 shows the high-resolution TEM (a), nanobeam electron diffraction pattern (b) taken from the region D and the nanobeam EDX profiles, (c–f) taken from the regions A, B, C, and D, respectively, of the $Fe_{56}Co_7Ni_7Zr_8Nb_2B_{20}$ alloy heated to 920 K corresponding to the temperature just above the first exothermic peak. Distinct fringe contrast is seen in the grains A, B, and C, while the D region consists only of a modulated contrast. The electron diffraction pattern B shows a halo-like ring, indicating that the region D is composed of an amorphous phase. It is clearly seen that the Co and Ni elements are dissolved into all the constituent phases. From the nanobeam EDX and EELS analyses, the A, B, and C are analyzed to be $Fe_{76}Nb_6B_{18}$, α-Fe, and Fe_2Zr, respectively. Besides, the Co and Ni contents appear to be the highest in the Fe_2Zr phase. Consequently, their crystalline phases can be expressed as

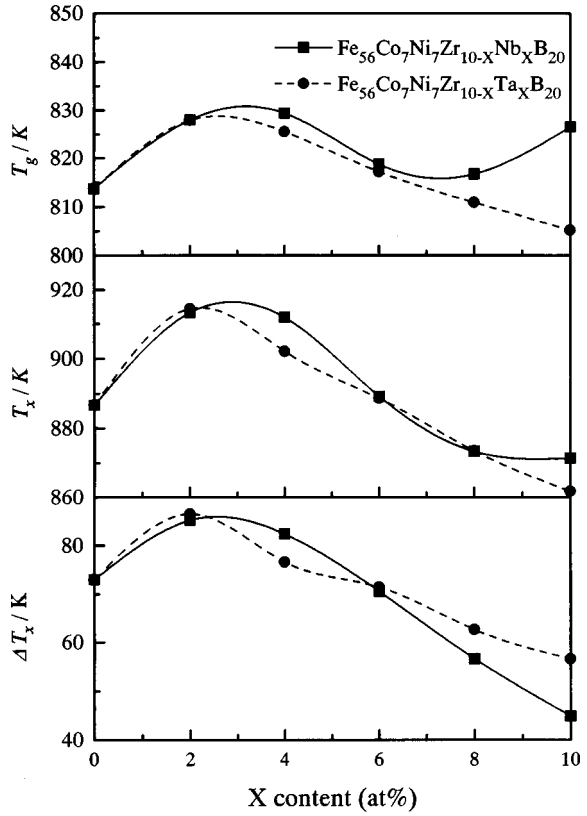

FIG. 5. Changes in the glass transition temperature (T_g), onset temperature of crystallization (T_x), and temperature interval of supercooled liquid region ($\Delta T_x = T_x - T_g$) as a function of Nb or Ta content for the amorphous $Fe_{56}Co_7Ni_7Zr_{10-x}Nb_xB_{20}$ and $Fe_{56}Co_7Ni_7Zr_{10-x}Ta_xB_{20}$ alloys.

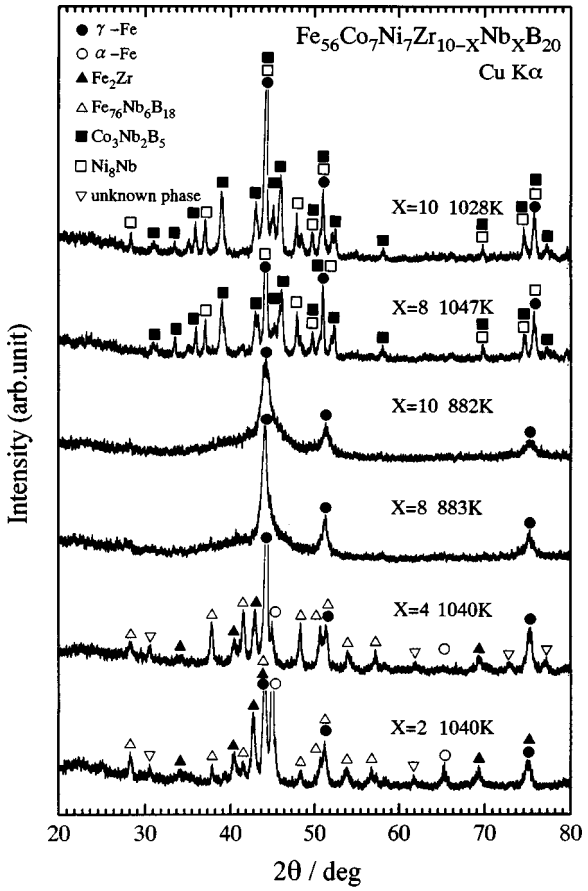

FIG. 6. X-ray diffraction patterns of the amorphous $Fe_{56}Co_7Ni_7Zr_{10-x}Nb_xB_{20}$ ($x = 2$, 4, 8, and 10 at. %) alloys annealed for 600 s at the temperatures just above the exothermic peaks.

$(Fe,Co,Ni)_{76}Nb_6B_{18}$, α-(Fe,Co,Ni), and $(Fe,Co,Ni)_2Zr$. However, the Fe content is much higher and hence the feature of their crystalline phases seems to be fully expressed even by the simple chemical formula such as $Fe_{76}Nb_6B_{18}$, α-Fe, and Fe_2Zr.

Similar crystallization behavior is also recognized for the $Fe_{56}Co_7Ni_7Zr_{10-x}Ta_xB_{20}$ amorphous alloys, as identified for the x-ray diffraction patterns shown in Fig. 9. The crystallization behavior takes place in the processes of amorphous→amorphous $+\alpha$-Fe$+\gamma$-Fe$+$FeB→α-Fe$+\gamma$-Fe $+$FeB$+Fe_2Zr$ for the alloys containing less than about 7 at.% Ta and amorphous→amorphous$+\gamma$-Fe→γ-Fe$+$FeB$+Ni_3B+Ni_8Ta$ for the alloys above 8 at.% Ta. Here, one can notice that the fully crystallized phases are composed of the Ni-rich and Ta-poor phases, in spite of nearly the same concentrations of Ni and Ta. In order to confirm the dissolution of Ta element into the amorphous phase, the EPMA profiles of the amorphous $Fe_{56}Co_7Ni_7Zr_{10-x}Ta_xB_{20}$ ($x = 2$, 4, 8, and 10 at .%) alloys are shown in Fig. 10. The intensity of the crystalline Ta peaks increases steadily with increasing nominal Ta content. This result indicates that the Ta element is surely dissolved into the amorphous phase in spite of its high melting temperature. The absence of the Ta-rich compound may be due to the dissolution of a large amount of Ta into the γ-Fe phase. That is, the diffusivity of Ta at the crystallization temperature is too low to form an equilibrium compound with high Ta concentrations. The dissolution of a large amount of Ta seems to cause an increase in the precipitation tendency of the γ-Fe phase. This presumption also implies that the crystalline structure does not always reach an equilibrium state in the $Fe_{56}Co_7Ni_7Zr_2Ta_8B_{20}$ alloy containing the high-melting temperature elements.

Judging from the data[25] on the negative heat of mixing for the atomic pairs among the constituent elements, it is thought that the bonding force is considerably smaller for the Fe–Nb and Fe–Ta pairs than for the other atomic pairs. The smaller bonding nature of Fe–Nb and Fe–Ta pairs is thought to allow the generation of isolated Fe–Fe bonding pairs, leading to the change in the first-stage crystalline structure from α-Fe$+\gamma$-Fe$+Fe_{76}Nb_6B_{18}$ to γ-Fe for the alloys containing more than 8% Nb (or Ta). A more detailed discussion on this point will be given in the next section. The DSC curves shown in Figs. 3 and 4 are believed to be the first evidence for the appearance of the wide supercooled liquid region above 45 K in the amorphous alloys where the crystallization occurs with two distinct stages and the temperature interval of the two exothermic peaks is as large as about 150 K.

Figure 11 shows hysteresis I–H loops of the $Fe_{56}Co_7Ni_7Zr_{10-x}Nb_xB_{20}$ amorphous alloys subjected to annealing for 300 s at 800 K just below T_x. It is seen that the replacement of Zr by Nb causes a decrease in I_s from 0.96 T at 0% Nb to 0.61 T at 10% Nb through 0.75 T at 2 at. % Nb,

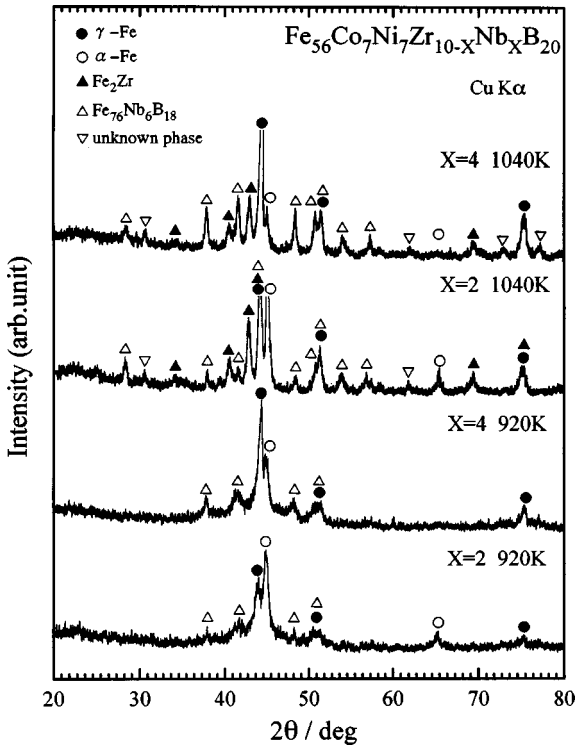

FIG. 7. X-ray diffraction patterns of the amorphous $Fe_{56}Co_7Ni_7Zr_{10-x}Nb_xB_{20}$ ($x=2$ and 4 at. %) alloys annealed for 600 s at 920 K. The data of the alloys annealed for 600 s at 1040 K are also shown for comparison.

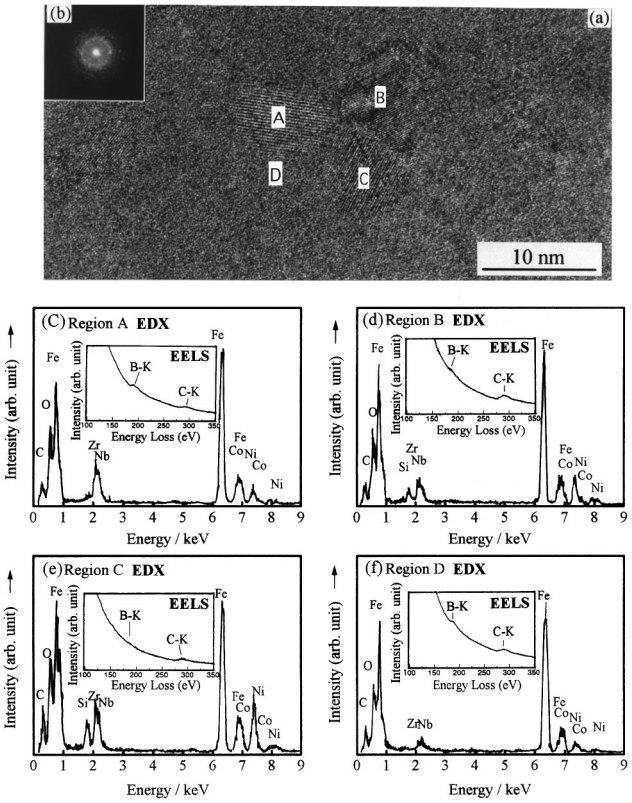

FIG. 8. High-resolution TEM image (a), nanobeam electron diffraction pattern (b) taken from the region D, and nanobeam EDX and EELS profiles (c–f) taken from the regions A, B, C and D in (a), respectively, for the amorphous $Fe_{56}Co_7Ni_7Zr_8Nb_2B_{20}$ alloy annealed for 600 s at 1040 K.

while the H_c shows low values of 1.1–2.0 A/m and does not have appreciable compositional dependence. Although the total content of Fe and Co elements remains constant, the I_s decreases by 0.21 T only by the addition of 2% Nb. The change in I_s with Nb content seems to reflect the change in Curie temperature (T_c). The hysteresis I–H loops for the $Fe_{56}Co_7Ni_7Zr_{10-x}Ta_xB_{20}$ amorphous alloys shown in Fig. 12 also show similar change with Ta content. The I_a decreases gradually from 0.96 to 0.71 T in the range up to 6% Ta and increases to 0.85 T at 8% Ta, while the H_c keeps the low values of 2.0–2.7 A/m in the whole Ta content range. Figure 13 shows changes in effective permeability (μ_e) at 1 kHz and saturated magnetostriction (λ_a) as a function of Nb or Ta content for the $Fe_{56}Co_7Ni_7Zr_{10-x}Nb_xB_{20}$ and $Fe_{56}Co_7Ni_7Zr_{10-x}Ta_xB_{20}$ amorphous alloys in as quenched and annealed (300 s, 800 K) states, together with the data of I_s and H_c. It is seen that the H_c and μ_e are significantly improved by the annealing treatment, though no distinct changes in I_s and λ_e are recognized. The maximum μ_e for the annealed samples reaches 25 000 at 2% Nb and 16 700 at 8% Ta. The compositions showing the maximum μ_e values agree with those for I_s. The λ_a is in the range of 7×10^{-5}–12×10^{-6} for the Nb-containing alloys and 12×10^{-6}–15×10^{-6} for the Ta-containing alloys, being slightly lower for the former alloys. Figure 14 shows change in T_c as a function of Nb or Ta content for the $Fe_{56}Co_7Ni_7Zr_{10-x}Nb_xB_{20}$ and $Fe_{56}Co_7Ni_7Zr_{10-x}Ta_xB_{20}$ amorphous alloys subjected to annealing for 300 s at 800 K. The T_c decreases monotonously from 594 to 447 K with increasing Nb content from 0 to 10% Nb. However, the change in T_c as a function of Ta is slightly different from that for the Nb-containing alloy. That is, the T_c decreases significantly to 503 K at 2% Ta and then increases gradually in the Ta content range up to 6 at .% and significantly to 538 K at 8% Ta. The compositional dependence of T_c for these alloy series is analogous to that for I_s and hence an alloy design leading to the increase in T_c is concluded to be an effective method for an increase in I_s. From the compositional dependence of the thermal stability of the supercooled liquid and the magnetic properties, it is concluded that the $Fe_{56}Co_7Ni_7Zr_{10-x}M_xB_{20}$ (M=Nb or Ta) amorphous alloys containing 2% Nb or 8% Ta have the combination of large glass-forming ability and good soft magnetic properties.

IV. DISCUSSION

It was shown in Figs. 3 and 4 that the replacement of Zr by 2–4% Nb (or Ta) causes the significant extension of the supercooled liquid region before crystallization by the increase in T_x exceeding the degree of the increase in T_x as a function of Nb or Ta content. It is to be noticed that the largest ΔT_x values of 85 K at 2% Nb and 87 K at 2% Ta are larger by about 20 K than the largest value (66 K for Fe–(Al, Ga)–Nb–(P,C,B,Si) system)[26] in Fe-based amorphous alloys reported-hitherto. The significant increase in ΔT_x allows us to expect that the new Fe–Co–Ni–Zr–Nb–B and Fe–Co–Ni–Zr–Ta–B alloys have a large glass-forming ability which enables the production of bulk amorphous alloys with diam-

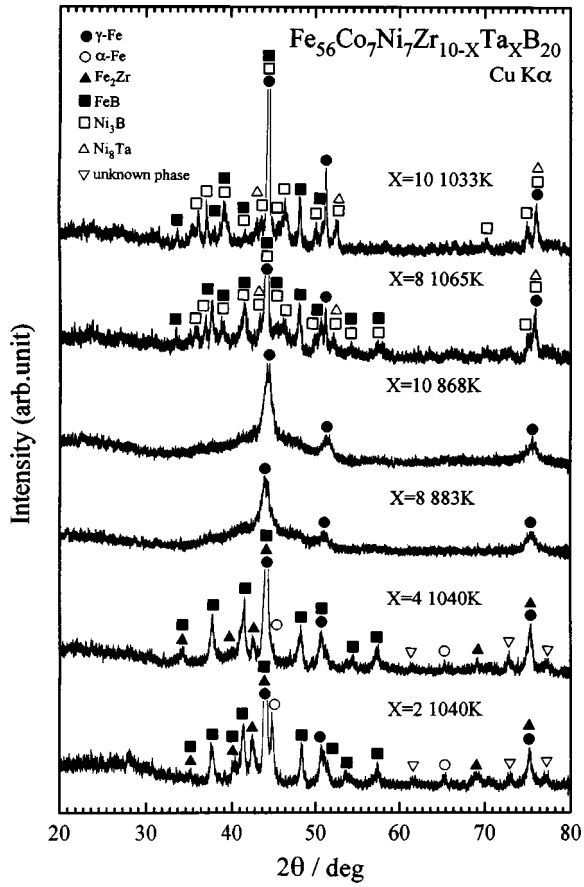

FIG. 9. X-ray diffraction patterns of the amorphous $Fe_{56}Co_7Ni_7Zr_{10-x}Ta_xB_{20}$ ($x=2$, 4, 8, and 10 at. %) alloys annealed for 600 s at the temperatures just above the exothermic peaks.

eters above several millimeters by the copper mold casting process. Consequently, it is important to discuss the reason for the significant extension of the supercooled liquid region before crystallization by the addition of 2–4% Nb (or Ta). It has previously been pointed out that the appearance of the

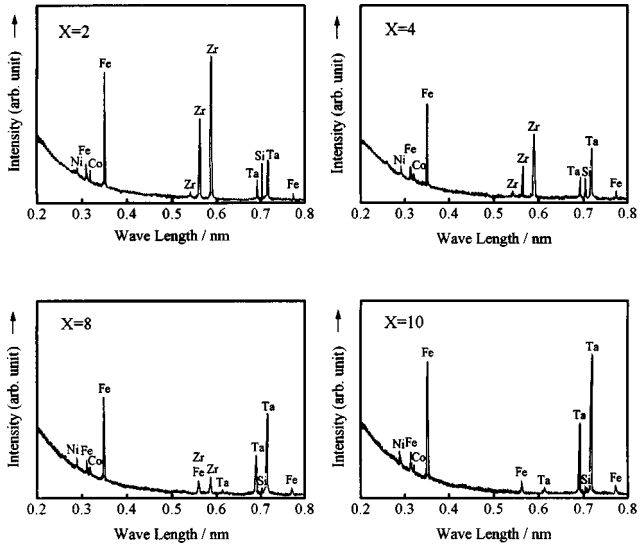

FIG. 10. Electron probe microanalysis (EPMA) profiles of the as-quenched amorphous $Fe_{56}Co_7Ni_7Zr_{10-x}Nb_xB_{20}$ ($x=2$, 4, 8, and 10 at. %) alloys.

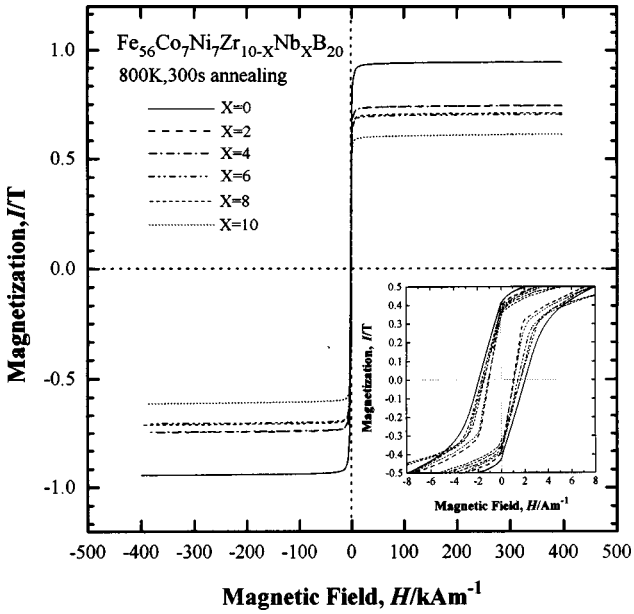

FIG. 11. Hysteresis I–H loops of the amorphous $Fe_{56}Co_7Ni_7Zr_{10-x}Nb_xB_{20}$ alloys annealed for 300 s at 800 K.

wide supercooled liquid region of 73 K[20] for the Fe–Co–Ni–Zr–B alloys without Nb or Ta is due to the satisfaction of the three empirical rules for the achievement of large glass-forming ability, namely, (1) a multi-component system consisting of more than three constituent elements, (2) significantly different atomic size ratios above about 12% among the three main constituent elements, as is evidenced from the change Zr≫Fe>Co=Ni≫B[7] and (3) large negative heats of mixing among the main constituent elements, as is evidenced from the predicted negative enthalpies of mixing of 37–72 kJ/mol atom for Fe–Zr, Co–Zr, and Ni–Zr pairs, 33–38 kJ/mol atom for Fe–B, Co–B, and Ni–B pairs and 102 kJ/mol atom for the Zr–B pair.[25] The addition of an appropriate amount (2–4 at. %) of Nb or Ta is expected to cause an enhancement of the degree of the satisfaction of the three empirical rules. That is, the atomic size changes more

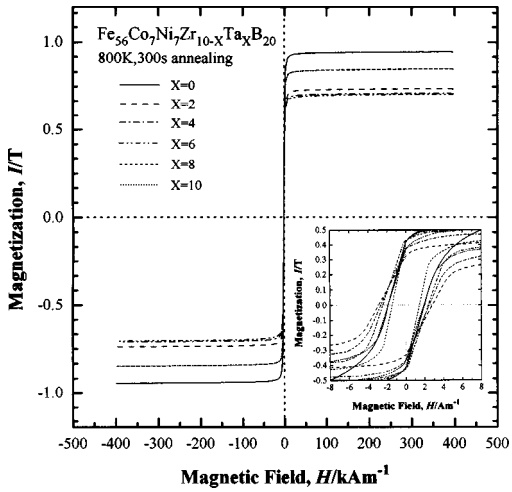

FIG. 12. Hysteresis I–H loops of the amorphous $Fe_{56}Co_7Ni_7Zr_{10-x}Ta_xB_{20}$ alloys annealed for 300 s at 800 K.

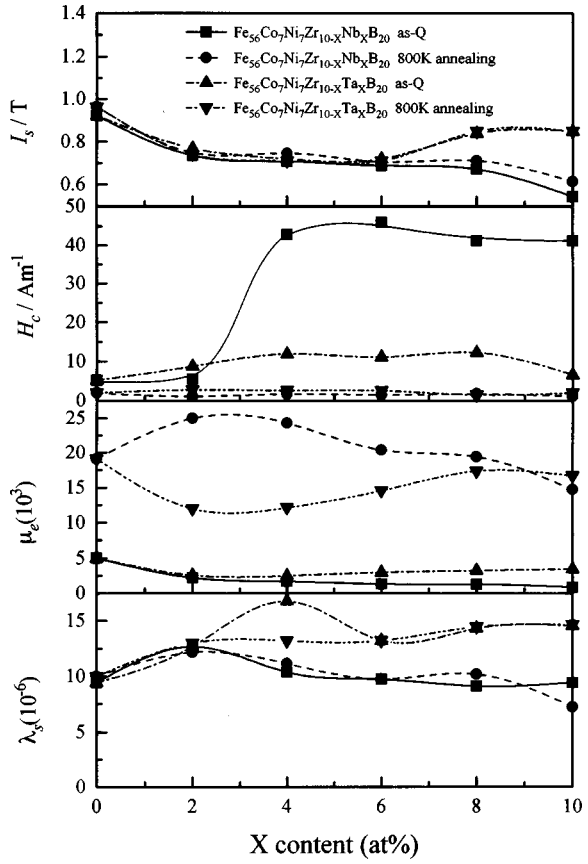

FIG. 13. Changes in saturation magnetization (I_s), coercive force (H_c), permeability at 1/kHz (μ_e) and saturated magnetostriction (λ_s) as a function of Nb or Ta content for the amorphous $Fe_{56}Co_7Ni_7Zr_{10-x}Nb_xB_{20}$ and $Fe_{56}Co_7Ni_7Zr_{10-x}Ta_xB_{20}$ alloys in as-quenched and annealed (300 s, 800 K) states.

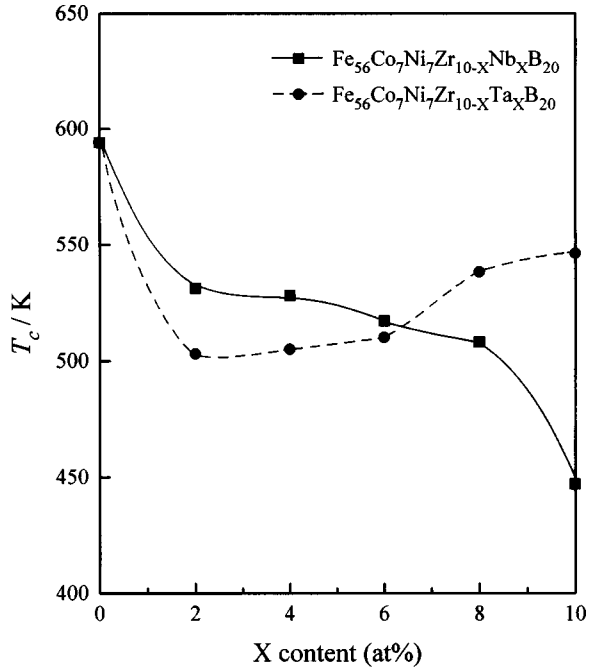

FIG. 14. Changes in T_c with Nb or Ta content for the amorphous $Fe_{56}Co_7Ni_7Zr_{10-x}Nb_xB_{20}$ and $Fe_{56}Co_7Ni_7Zr_{10-x}Ta_xB_{20}$ alloys annealed for 300 s at 800 K.

continuously in the order of Zr≫Nb (or Ta)≫Fe>Co =Ni≫B[27] and additional atomic pairs of Fe–Nb (or Ta), Co–Nb (or Ta), Ni–Nb (or Ta), and Nb (or Ta)–B with large negative heats of mixing generate for the Nb- or Ta-containing alloys. The increase in the degree of the satisfaction of the three empirical rules may be the reason for the extension of the supercooled liquid region before crystallization by the addition of 2–4% Nb (or Ta). However, the predicted heat of mixing is 23–45 kJ/mol atom for the Fe–Nb, Co–Nb and Ni–Nb pairs, 22–44 kJ/mol atom for the Fe–Ta, Co–Ta, and Ni–Ta pairs, 79 kJ/mol atom for the Nb–B pair, and 78 kJ/mol atom for the Ta–B pair.[25] These heats of mixing for the atomic pairs containing Nb or Ta element are considerably smaller than those for the corresponding Fe–Zr, Co–Zr, Ni–Zr, and Zr–B pairs. The weaker bonding nature of the main Fe–Nb or Fe–Ta atomic pair seems to result in the decrease in ΔT_x for the alloys containing more than 8 at. % Nb (or Ta), accompanying the change in the primary precipitation from α-Fe+γ-Fe+$Fe_{76}Nb_6B_{18}$ (α-Fe+γ-Fe +FeB) to γ-Fe. This change indicates the importance of the attractive bonding nature among the constituent elements for the achievement of the wide supercooled liquid region before crystallization, in addition to the significantly different atomic size ratios.

V. SUMMARY

With the aim of searching for a new amorphous alloy with a wide supercooled liquid region before crystallization and good soft magnetic properties, the compositional dependence of T_g, T_x, ΔT_x, crystallization behavior and magnetic properties was examined for the alloy series of $Fe_{56}Co_7Ni_7Zr_{10-x}Nb_xB_{20}$ and $Fe_{56}Co_7Ni_7Zr_{10-x}Ta_xB_{20}$ (x $=0-10$ at. %). The results obtained are summarized as follows.

(1) The glass transition and subsequent supercooled liquid region were observed in the temperature range before crystallization for all the alloys. The T_g and T_x are 814 and 887 K, respectively, for the 10% Zr alloy, increase by the addition of Nb or Ta and show maximum values of 828 and 913 K, respectively, for the 2–4% Nb alloys and 827 and 914 K, respectively, for the 2–4% Ta alloys. The degree of the increase in T_x as a function of Nb or Ta content is larger than that for T_g, leading to the maximum ΔT_x of 85 K for the 2% Nb alloy and 87 K for the 2% Ta alloy. These values are larger by about 20 K than the largest value for Fe-based amorphous alloys reported hitherto.

(2) The crystallization of the Nb (or Ta)-containing alloys takes place through two stages of amorphous (Am) $\rightarrow$Am′+α-Fe+$Fe_{76}Nb_6B_{18}$(Am+α-Fe+γ-Fe+FeB)$\rightarrow$$\alpha$-Fe +$\gamma$-Fe+$Fe_{76}Nb_6B_{18}$+$Fe_2Zr$($\alpha$-Fe+$\gamma$-Fe+FeB+$Fe_2Zr$) for the alloys containing less than about 6% Nb (or Ta) and Am$\rightarrow$Am′+γ-Fe+$Co_3Nb_2B_5$+Ni_8Nb (or γ-Fe+FeB +Ni_3B+Ni_8Ta) for the alloys containing more than 8% Nb (or Ta). The temperature interval of the two exothermic peaks is as large as about 150 K for the 8 and 10% Nb (or Ta) alloys. It is to be noticed that the wide supercooled liquid region above 50 K appears even for the alloys with the dis-

tinct two-stage crystallization processes in which the primary crystalline phase consists only of γ-Fe phase.

(3) The I_s, H_c and μ_e at l kHz in the optimally annealed state are 0.96 T, 2.0 A/m, and 19 100, respectively, for the Fe–Co–Ni–Zr–B alloy. The increase in Nb content causes the monotonous decrease in I_s to 0.61 T at 10% Nb and the increase in μ_e to 25 000 at 2% Nb, followed by the decrease to 14 800 at 10% Nb. The Ta-containing alloy shows maximum values of 0.85 T for I_s and 17 400 for μ_e at 8% Ta. The H_c keeps low values of 1.1–2.7 A/m in the whole Nb or Ta content range and the λ_s is in the range of 7×10^{-6}–15×10^{-6} for both alloys. The T_c is 594 K for the 10% Zr alloy, 531 K for the 2% Nb alloy, and 538 K for the 8% Ta alloy.

(4) The alloys containing 2% Nb or 8% Ta exhibit the good combination of the wide supercooled liquid region and good soft magnetic properties. The finding of the new amorphous alloys with the two characteristics is important for the future development of bulk amorphous alloys in the application of soft magnetic materials.

ACKNOWLEDGMENT

The authors are grateful to the Grant-in-Aid for Specially Promoted Research of The Ministry of Education, Science, Sports and Culture, for support of this research.

[1] A. Inoue, K. Kita, T. Zhang, and T. Masumoto, Mater. Trans. JIM **30**, 722 (1989).
[2] A. Inoue, T. Zhang, and T. Masumoto, Mater. Trans. JIM **31**, 425 (1990).
[3] A. Inoue, T. Nakamura, T. Sugita, T. Zhang, and T. Masumoto, Mater. Trans. JIM **34**, 351 (1993).
[4] A. Inoue, A. Kato, T. Zhang, S. G. Kim, and T. Masumoto, Mater. Trans. JIM **32**, 609 (1991).
[5] A. Inoue, T. Nakamura, N. Nishiyama, and T. Masumoto, Mater. Trans. JIM **33**, 937 (1992).
[6] A. Inoue, T. Saito, H. Yamamoto, and T. Masumoto, J. Mater. Sci. Lett. **12**, 946 (1993).
[7] A. Inoue, T. Zhang, N. Nishiyama, K. Ohba, and T. Masumoto, Mater. Trans. JIM **34**, 1234 (1993).
[8] A. Inoue, T. Shibata, and T. Zhang, Mater. Trans. JIM **36**, 1420 (1995).
[9] A. Peker and W. L. Johnson, Appl. Phys. Lett. **63**, 2342 (1993).
[10] A. Inoue, N. Nishiyama, and T. Matsuda, Mater. Trans. JIM **37**, 181 (1996).
[11] A. Inoue, Y. Shinohara, and J. S. Gook, Mater. Trans. JIM **36**, 1427 (1995).
[12] A. Inoue, A. Takeuchi, T. Zhang, and A. Murakami, IEEE Trans. Magn. **32**, 4866 (1996).
[13] T. Zhang, A. Inoue, and T. Masumoto, Mater. Trans. JIM **32**, 1005 (1991).
[14] A. Inoue, T. Zhang, and T. Masumoto, J. Non-Cryst. Solids **156-158**, 473 (1993).
[15] A. Inoue, Mater. Trans. JIM **36**, 866 (1995).
[16] A. Inoue, in *Nanostructured and Non-Crystalline Materials*, edited by M. Vazquez and A. Hernando (World Scientific, Singapore, 1995), p. 15.
[17] A. Inoue, in *Advanced Materials and Processing*, edited by K. S. Shin, J. K. Yoon, and S. J. Kim (Korean Inst. Metals and Materials, Seoul, 1995), p. 1849.
[18] A. Inoue, Mater. Sci. Forum **179–181**, 691 (1995).
[19] A. Inoue, Sci. Rep. Res. Inst. Tohoku Univ A **42**, 1 (1996).
[20] A. Inoue, T. Zhang, T. Itoi, and A. Takeuchi, Mater. Trans. JIM **38**, 358 (1997).
[21] A. Inoue, H. Koshiba, and T. Zhang, Mater. Trans. JIM **38**, 577 (1997).
[22] A. Inoue, T. Zhang, and A. Takeuchi, Appl. Phys. Lett. **71**, 464 (1997).
[23] *Materials Science of Amorphous Alloys*, edited by T. Masumoto (Ohmu, Tokyo, 1981), p. 97.
[24] C. H. Smith, in *Rapidly Solidified Alloys*, edited by H. H. Liebermann (Dekker, New York, 1993), p. 617.
[25] F. R. de Boer, R. Boom, W. C. M. Mattens, A. R. Miedema and A. K. Niessen, *Cohesion in Metals* (Elsevier, Amsterdam, 1988).
[26] A. Inoue, Y. Shinohara, and J. S. Gook, Mater. Trans. JIM **36**, 1427 (1995).
[27] *Metals Databook*, edited by the Japan Institute of Metals (Maruzen, Tokyo, 1983), p. 12.